

Numerical investigation of cavitation performance of slotted hydrofoil for amphibious aircraft

Fernando Roca Conesa¹⁾ *Rhea Patricia Liem²⁾

¹⁾ *Universitat Politècnica de València, Camino de Vera s/n, Valencia 46022, Spain*

²⁾ *Department of Mechanical and Aerospace Engineering, The Hong Kong University of Science and Technology, Hong Kong.*

¹⁾ frocaconesa@connect.ust.hk

²⁾ rpliem@ust.hk

ABSTRACT

The proposed study will focus on numerically investigating the performance of hydrofoil in the context of amphibious aircraft application. In particular, we also study the effectiveness of a slotted hydrofoil in minimizing the cavitation phenomenon, and thus improving the overall water takeoff performance of the amphibious aircraft. As a case study, we refer to the ICON A5 as our reference model. First, we propose an approach to estimate the hydrofoil surface and to determine which airfoil is most suitable in terms of preventing cavitation and providing a high hydrodynamic efficiency. Once the hydrofoil is chosen (Clark-Y), a 2-dimensional numerical study of the hydrodynamic and cavitating characteristics of a non-slotted hydrofoil is done in ANSYS Fluent. Two different parameters are used to detect the appearance of the different cavitation regimes, namely the incipient, and the cloud and partial cavitation regimes. To improve the performance, we propose a slotted hydrofoil to be a passive method to control the cavitation performance through the boundary layer control. Numerical results of several slotted configurations demonstrate notable improvement on the cavitation performance. A numerical research for cavitation number 0.7 (cloud cavitation regime) was carried in ANSYS Fluent and results prove that both cavitating and hydrodynamic performances can be improved.

Keywords: *Hydrofoil design, slotted hydrofoil, cavitation inhibition, passive flow control.*

Nomenclature

C_L	Lift Coefficient	A	Acceleration
S_H	Hydrofoil Area	ft	Feet
α	Angle of Attack (AoA)	cm	Centimetre
S_w	Wing Area	St	Strouhal number
V_{TO}	Take-off speed	ref	Reference
CFD	Computational Fluid Dynamics	Pa	Pascals
σ	Cavitation number	W_{TO}	Take off Weight
C_{Lmax}	Maximum Lift Coefficient	°	Degree
ρ	Density	α_l	Liquid volume fraction
L_h	Lift of the hydrofoil	C_{Pmin}	Minimum Pressure Coefficient
L_w	Lift of the wing	X_{CPmin}	x position when C_{Pmin} is reached
W	Weight	C_D	Drag Coefficient
g	Gravity	α_v	Vapor volume fraction
m	Mass	SST	Menter's Shear Stress Transport

¹⁾ Assistant Professor, Ph.D.

²⁾ Aerospace Engineering Graduate Student

1. Introduction

Amphibious aircraft can take off and land on both water and conventional runways on land airports. One of the main interest in developing these types of aircrafts lie in the ability of transporting passengers and cargo to the remotest parts of countries with very long coastlines or with many islands, where it is impractical to build airports and runways. In addition, amphibious aircraft can be used in emergency situations such as rescue missions and aerial firefighting or even for recreation purposes. An amphibious aircraft needs to be able to take off and landing in both water and land. Normally, amphibious aircraft need to take off in a short distance (e.g. rivers, ports) so attention must be paid to take off performance. One of the main challenge is to reduce water take off distance. To minimise that a hydrofoil can be used. A hydrofoil is similar to an airfoil (a lift generating device) but works underwater. This device can provide extra lift and reduce drag during the water take off. The advantage of the hydrofoil is that it can get the hull out of the water, allowing a faster take off with a shorter distance. By lifting the hull out of the water, the aircraft needs to only overcome the drag on the foils instead of all the drag on the hull, and thus allows a higher rate-of-climb.

Some of the problems with the use of hydrofoils are detailed in Petrie's report [1] on the developmental and operational experiences with the United States Navy's first hydrofoil ship. During the testing of the ship in 1961, it was found that there was cavitation damage in the aft propellers due to separation off the upper surface of the hydrofoil. Cavitation occurs when the water pressure drops below the vapor pressure of the working liquid. When this phenomenon appears, the hydrofoil no longer generates enough lift, which could lead to a catastrophic impact of the aircraft onto the water. As the velocity increases during take-off, the pressure on the upper surface of the hydrofoil decreases and could drop below the sea water vapour pressure, leading to cavitation. This phenomenon also affects the structural integrity of the hydrofoil and could generate vibrations, erosion, or noise problems. In addition, the hydrodynamic drag increases with cavitation, so it can lead to significant performance decay. Therefore, preventing cavitation is the primary consideration in the design of the hydrofoil system and it is the scope of the present study.

The flow separation control and boundary layer control are methods for the boundary layer management aimed to reduce cavitation and improve the performance. Boundary layer control methods can be divided into passive or active methods. The active flow separation control requires additional energy for the boundary layer control. A variable sweep hydrofoil [2] is an active method which can be used to improve hydrodynamic and cavitation performance. Among the active methods, cavitating flow control through continuous tangential mass injection through a slot channel in the guided vanes section surface of a hydrofoil was proposed by Mikhail V. Timoshevskiy et al. [3] to reduce substantially the amplitude or and suppress the periodic cavity length oscillations and pressure pulsations. Vortex generators are passive flow control solutions. An appendage located on the hydrofoil wall was proposed by M.Mortezazadeh et al. [4] as a passive method to decrease the size of the bubble during cavitation phenomena and control the boundary layer over the hydrofoil. Hydrofoil steering vanes and surface texture variation were proposed by T.B.Hilleman [5] to reduce underwater drag and cavitation reduction. The use of a slot to control the boundary layer is passive flow control solution. The slotted hydrofoil was firstly introduced by NASA [6] in airfoils to increase the laminar flow region over the airfoil and thus achieve a drag reduction for Business-jet-applications. Other authors (R. Belamadi et al [7]) have applied this passive method to improve the aerodynamic performance of wind turbine blades, but the first application to this passive

method into hydrofoils was performed by Wei Qun (2014) [8]. In their study, they used a vice foil to improve cavitation and hydrodynamic performance. However, they optimize the position of the vice foil, for a fixed slot geometry, they do not focus on the design of the slot itself.

The list of the boundary layer control methods provided is not exhaustive. The advantages of a passive method are that it does not need an external mechanism for its operation which could substantially reduce the manufacturing cost and time. In other words, a passive control does not require auxiliary power or a control loop, which could help to a weight reduction. The present work focuses on a numerical investigation of a slotted hydrofoil to improve notably the cavitation and hydrodynamic performance. Different slot locations, slot widths and angles are studied to achieve this objective for a hydrofoil for amphibious aircrafts applications using 2D simulations.

This paper is organized as follows. Section 2 describes an iterative method used to estimate the hydrofoil surface and the criteria followed to select the airfoil shape for the hydrofoil. Section 3 introduces in detail the numerical analysis for the amphibious aircraft hydrofoil. The corresponding results are shown in Section 4. Section 5 proposes a slotted hydrofoil to improve cavitation performance and shows the numerical results. Concluding remarks are given in Section 6.

2. Iterative approach for foil and chord selection

A hydrofoil refers to a wing structure mounted on a strut below the amphibious aircraft. This lifting generating device is used to lift the hull out of the water during water take-off and allows a drag reduction and a notably increase in the rate-of-climb. To size and design the hydrofoil, ICON A5 amphibious aircraft is taken as reference. ICON A5 is a high-wing monoplane with its wing and fuselage made up of carbon-fibre material. Its Dornier-style sponsons provide a high hydrodynamic stability. To determine the most suitable foil for the hydrofoil an iterative method has been proposed. It is assumed that there is no taper ratio in our design. ICON A5 specifications can be found in Table 1.

Table 1. ICON A5 main specifications[†].

Weight (kg)	686
Airfoil surface (m ²)	13.46
Stall speed -clean flaps- (m/s)	20.06
Take-off distance (m)	256
Take-off speed (m/s)	24

Vertical acceleration of the amphibious aircraft takes an important role during take-off. To determine the hydrofoil surface kinematic Eq. (2.1) has been used to consider the forces in vertical direction. Eq. (2.1) is based on Newton's second law, which states that during take-off, the lift provided by the hydrofoil and wing minus the weight of the model aircraft is equal to the model aircraft mass multiplied by the vertical acceleration. Water take-off can be decomposed into several stages. Before the amphibious aircraft starts to rotate at the last stage of the take-off process (when the aft hull is free from water), the amphibian reaches the hump speed. The hump speed is defined at the point when the hull waterline tends to stagnate, and the static

[†] Data available online at [http:// www.planeandpilotmag.com/article/icon-a5/](http://www.planeandpilotmag.com/article/icon-a5/) [retrieved 10 May 2018].

buoyant force and hydrodynamic drag force reach the maximum value. Shortly after the amphibious aircraft reach the hump speed, a rapid disappearance of the hull buoyant force occurs [8]. Since cavitation phenomena will appear at a high speed (after the hump speed), when the buoyant force is relatively small compared with the other lift contributions, the buoyancy has been neglected in Eq. (2.1).

The lift of the hydrofoil and wing is provided by Eqs. (2.2) and (2.3), respectively. The C_L of the wing at take-off condition can be obtained by Eq. (2.4), since stall speed is known from ICON A5 specifications (see Table 1). Since the take-off distance, take-off speed and the final altitude of the amphibious aircraft at take-off is known, it is possible to obtain the vertical acceleration during take-off (assuming a uniformly accelerated rectilinear motion, with constant acceleration). So, the unknowns of Eq. (2.1) are the hydrofoil area, and the C_L of the hydrofoil (which strongly depends on the angle of attack, α). As it has been assumed that there is no taper ratio, the hydrofoil area only depends on the chord and span. An iterative process has been carried to obtain the hydrofoil surface. Firstly, an initial Reynolds number has been calculated (Eq. (2.5)) and using XFOIL the lift coefficient of the hydrofoil has been obtained (for an AoA of 3°). The XFOIL code combines a panel method and an integral boundary layer formulation for the analysis of potential flow around the airfoils. Iterations has been done (with different chords values) until the convergence of the Reynolds number (the Reynolds number obtained with the chord after solving Eq. (2.1) is the same as the one used in XFOIL to obtain the C_L of the hydrofoil). This iterative process has been carried for several types of foils.

$$L_h + L_w - W = ma \quad (2.1)$$

$$L_h = \frac{1}{2} (V_{TO})^2 C_{Lh} S_h \rho_{water} \quad (2.2)$$

$$L_w = \frac{1}{2} (V_{TO})^2 C_{LTO} S_w \rho_{air} \quad (2.3)$$

$$V_{TO} = 1.2 V_{Stall} = \sqrt{\frac{2W_{TO}}{C_{LTO} S_w \rho_{air}}} \quad (2.4)$$

$$Re = \frac{\rho_{water} V_{TO} c}{\mu_{water}} \quad (2.5)$$

Several types of foils have been studied to determine which one is most suitable in terms of preventing cavitation and providing a high hydrodynamic efficiency. The studied foils are: Clark-Y, NACA 0009, NACA 63-412, YS-930, Selig S1223, AH21-7, E-818, E-851, HQ,309, HQ-2195, MH-121 and MH-122. The applications of all these foils are related to hydrodynamic applications [10,11,12,13]. Hydrofoil surface for each foil candidate after the iteration process is shown in Table 2. Once the chord for each foil mentioned above is known, a viscous flow simulation is done in XFOIL to obtain C_L , C_D , C_{Pmin} and X_{CPmin} for each airfoil at a range of angles of attack (between -3° and 10°). To prevent cavitation, which is our main design requirement, the local pressure of the whole upper surface of the hydrofoil must be higher than the vapor pressure. In other words, the minimum pressure coefficient (C_{Pmin}) of the hydrofoil must be higher than a certain value. To determine the most suitable foil our reference amphibious aircraft, four parameters have been evaluated: C_{Pmin} , C_L/C_D , C_L/C_{Pmin} and Δ_{CPmin} vs AoA. All these parameters have been evaluated at an angle of attack of 3° , assuming that the take-off is at this AoA. The first parameter listed is relevant to assess which hydrofoil is closer to cavitation phenomena at take-off condition. C_L/C_D ratio is a measure of the hydrodynamic efficiency and thus, this parameter has a high influence on the take-off performance. C_L/C_{Pmin} provides a measure of the decrease of the pressure (and thus, the tendency to cavitation) when the lift increases. Finally, Δ_{CPmin} vs AoA provides the rate of decrease of minimum pressure

coefficient with the increase of angle of attack. Wherein the importance of $\Delta_{C_{Pmin}}$ vs AoA is set higher among all the study parameters, because the angle of attack could increase easily during take-off due to waves impacts, or other external phenomena, and thus, the minimum pressure coefficient will decrease (cavitation may occur) leading to a lift lose and vibrations. Therefore, it is important to consider how much would the pressure decrease as AoA increases. Table 3 shows the absolute value of these four parameters for each foil studied. The value of $|C_{Pmin}|$ is more beneficial (in terms of preventing cavitation) as low as possible. C_L/C_D ratio is better when it is as high as possible (i.e. more hydrodynamic efficiency). The value of $|C_L/C_{Pmin}|$ is more beneficial when it is as high as possible. Finally, the value of $|\Delta_{C_{Pmin}} \text{ vs AoA}|$ is better when it is as small as possible (good performance preventing minimum pressure drop as AoA increases). $\Delta_{C_{Pmin}}$ vs AoA has been calculated as the variation rate of C_{Pmin} between AoA 3° and 4° [‡]. As can be seen from Table 3, the values of C_L/C_D are considered to be very high. This may be due to the fact that XFOIL uses a combination of linear vorticity strength distribution with constant source strength on each panel in order to provide transpiration velocity values for viscous solver, therefore the accuracy of the results is limited by the resolution of the paneling [14]. Moreover, the transpiration velocities obtained from the potential flow code are essential to model sheet cavitation [15].

Table 2. Results of hydrofoil chord and span and C_L at take-off for each foil after the iteration process.

Parameters and Foils	ClarkY	NACA 0009	NACA 63412	YS930	S1223	AH217	E818	E851	HQ259b	HQ309	HQ2195	MH121	MH122
Hydrofoil chord (cm)	14.19	15.46	12.18	12.65	7.99	12.98	10.57	11.6	10.49	12.12	12.17	11.55	10.61
Hydrofoil span (cm)	24.7	50	30	30	20.1	30	32	33	34.5	28	32.5	29	28
C_L (take-off)	0.717	0.325	0.688	0.662	1.566	0.646	0.744	0.657	0.694	0.741	0.636	0.751	0.846

Table 3. Absolute value of the key decision parameters for each foil provided by XFOIL.

Parameters and Foils	ClarkY	NACA 0009	NACA 63412	YS930	S1223	AH217	E818	E851	HQ259b	HQ309	HQ2195	MH121	MH122
$ C_{Pmin}(3^\circ) $	1.077	1.225	1.092	1.590	1.963	1.246	2.715	1.820	1.131	1.044	1.143	1.753	1.232
$C_L/C_D(3^\circ)$	123.43	59.49	126.53	96.41	129.57	101.59	76.83	80.12	110.10	128.85	104.23	86.12	130.12
$ C_L/C_{Pmin}(3^\circ) $	0.666	0.266	0.630	0.416	0.798	0.519	0.272	0.361	0.614	0.710	0.556	0.429	0.683
$ \Delta_{C_{Pmin}} \text{ VS AoA}(\%) $	17.36	32.61	34.58	44.77	6.66	27.92	40.79	47.37	30.24	24.48	30.14	43.83	35.42

As can be extracted from Table 3, foil S1223 has the lower value of $|\Delta_{C_{Pmin}} \text{ vs AoA}|$, and the higher value of $|C_L/C_{Pmin}|$, so it seems to be the best choice among the rest. However, this airfoil goes into stall conditions when the AoA is approximately 5° , so it has been rejected since it could compromise the take-off performance. Other choices could be HQ-309 or Clark-Y as they have good hydrodynamic performance and a good behavior in preventing cavitation. Even though HQ-309 airfoil has a lower value of $|C_{Pmin}(3^\circ)|$, it is more sensitive to changes in C_{Pmin} when AoA increases (at 5° of AoA, $|C_{Pmin}|$ is higher in HQ-309 airfoil than in Clark-Y, which means that it is closer to cavitation). So, Clark-Y is the best option among all the foils which has been analyzed.

3. Numerical analysis

[‡] since S1223 approximately starts to stall at 5° AoA, the interval 3° - 4° has been chosen to evaluate $\Delta_{C_{Pmin}}$ vs AoA parameter.

The unsteady behaviour of cavitating flows and cavity shedding attract much attention during hydrofoil design stages since they seriously affect the hydrodynamic performance and hydrofoil integrity. Cavitation flow around a hydrofoil is often a multiphase flow associated with turbulence, unsteady flows, and phase change. Many researches have been carried out to simulate the cavitation flow and noticeable progresses have been made in recent years. Many experiences [8] have proven that CFD simulation can be used to analyse the cavitating behaviour successfully with coupling suitable cavitation and turbulence models. In order to figure out the cavitation performance of the Clark-Y hydrofoil numerical simulations were carried out in ANSYS Fluent.

3.1 Numerical setup

Figure 1 shows the airfoil shape which will be evaluated in ANSYS Fluent. Geometry was simplified to a 2-D problem. The computational domain and boundary conditions are illustrated in Figure 2. The Clark-Y hydrofoil is placed with an angle of attack equal to 3° . The computational domain stretches 3 chord lengths upstream (radius) and 14 chord lengths downstream. The inlet boundary condition is the specified take-off speed (24 m/s). Upper and lower boundaries are non-slip walls. The outlet is a constant pressure boundary condition defined by the cavitation number. The foil itself is a non-slip wall.

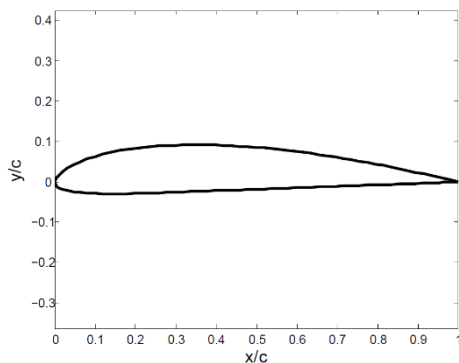


Figure 1. Clark-Y hydrofoil geometry.

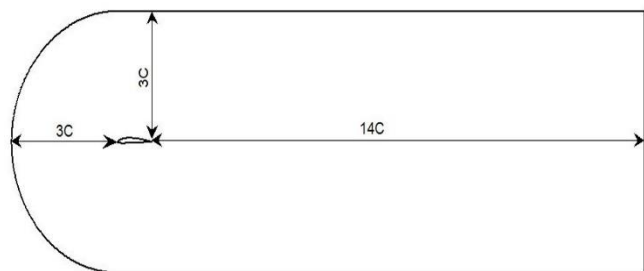


Figure 2. Outline of the 2D computational domain with boundary condition type showing.

Because of the unsteadiness of cavitating flow, the selection of the turbulence model is really critical for the accurate calculation of cavitation. The numerical model solved the unsteady Navier-Stokes equations, coupled with SST $k-\omega$ turbulence model, following the work by L.Qiu et al. [9], with automatic near-wall treatment which can automatically switch from wall functions to a low-Reynolds near wall formulation as the mesh is refined[§]. Unsteady simulations were carried out. A first order implicit transient formulation is used for the time-dependent computation. In the unsteady simulations, the time step is set as $\Delta t = 4.1 \times 10^{-6}$ s, which is chosen to assure an average Courant-Friendrichs-Lewy number of $CFL = U_\infty \Delta t / \Delta x = 1$, where Δx is the smallest grid size. In order to keep the balance between efficiency and computational accuracy, 20 iterations in each time step has been selected. The solving strategy used is the unsteady SIMPLE algorithm. PRESTO! and QUICK schemes are used for pressure and vapor phase transport equation respectively. To obtain an accurate resolution of the cavitation, second order discretization schemes are used for density, momentum, turbulent kinetic energy, and

[§] ANSYS Fluent documentation available online at <https://www.sharcnet.ca/Software/Ansys/17.0> [retrieved 10 May 2018].

dissipation rate. A least-squares-cell-based method is used to compute the gradients of the variables appearing in the governing equations.

3.2 Cavitation characterization

Cavitation process is normally characterized by a non-dimensional parameter called cavitation number (σ), as shows Eq. (3.2.1). This parameter is used to evaluate the potential for cavitation. In Eq. (3.2.1), p_v is the vapor pressure (which was set to 3540 Pa), ρ is the working liquid density, p_{ref} is the reference hydrostatic pressure and V is the free stream flow velocity. Every flow, whether cavitating or not, can be attributed to a cavitation number. The cavitation number depends on geometry, fluid temperature and inflow velocity [16]. Four different cavitation regimes can be observed in the flow over a body: incipient, sheet, cloud, and supercavitation. In cloud cavitation regime the vapour phase covers a subsection of the body [17]. The conditions at which cavitation first appears (the incipient regime) are described in Eq. (3.2.2) [18]. Where C_p is provided by Eq. (3.2.3), and p_{local} is the local fluid pressure. Lowering the value of the cavitation number will lead to the appearance of cavitation or in case that cavitation already exists, it will be extended.

$$\sigma = \frac{p_{ref} - p_v}{\frac{1}{2}\rho V^2} \quad (3.2.1)$$

$$\sigma + C_p \leq 0 \quad (3.2.2)$$

$$C_p = \frac{p_{local} - p_{ref}}{\frac{1}{2}\rho V^2} \quad (3.2.3)$$

To simulate cavitation Schnerr-Sauer model is used and thermal equilibrium between the liquid and vapor phases is assumed. This model expresses the vapour fraction as a function of the radius of the bubbles, which is assumed to be the same for all the bubbles. The governing equations describe the cavitation process involving a two-Eulerian phases system, where it is assumed that there is thermal equilibrium between all components and phases, and no-slip between any phase. In this work, two parameters are used to describe cavitation. The first one (Eq. (3.2.2)) indicates when incipient cavitation regime appears. In addition, the vapor volume fraction is used as an indicator of the appearance of the cloud cavitation regime.

3.3 Grid generation and independence study

In numerical simulations, the quality of the computational mesh has a great influence on the accuracy of the numerical results. The mesh should have adequate fineness to ensure the validity of the results. Mesh size near the wall has a key effect on the cavitation dynamics. The grid was generated by using an unstructured mesh. A large number of mesh elements are located near the hydrofoil surface to accurately capture the gradients in the boundary layer as well as the cavitation dynamics. In addition, a finer mesh has been done downstream, to capture the evolution and detachment of the vapor bubbles. The wall functions models need to adjust the thickness of neighboring cells to hydrofoil surface; the height of the first cell is $\Delta y = 1 \times 10^{-4}$ m to ensure that $y^+ \approx 1$, where $y^+ = yu_\tau/\nu$ is the non-dimensional wall distance (where y is the distance to the wall, u_τ is the friction velocity in the wall and ν is the local kinematic viscosity of the fluid). To take full advantage of SST k- ω turbulence model it is necessary to guarantee that $y^+ \approx 1$ (ANSYS Fluent Theory Guide, 2013). In the far-field area, the mesh resolution becomes progressively coarser since the flow gradients approach zero. To

model the evolution of the cavitation bubbles, a finer mesh is located close to the hydrofoil and trailing edge. Figure 3 and 4 shows the mesh details.

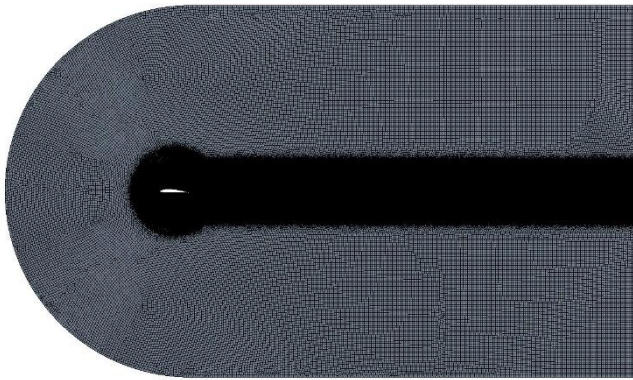


Figure 3. General view of the grid of Clark-Y hydrofoil.

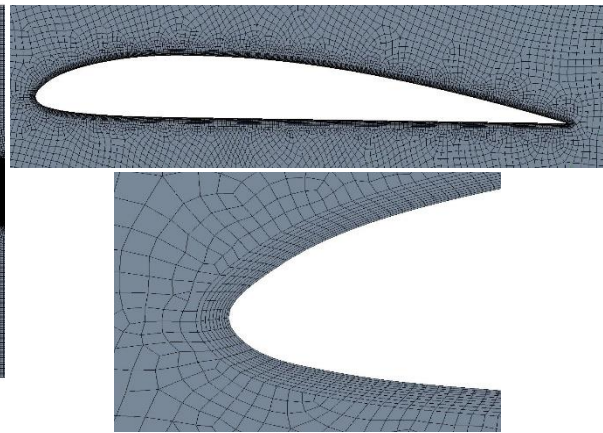


Figure 4. Hydrofoil and leading-edge mesh detail.

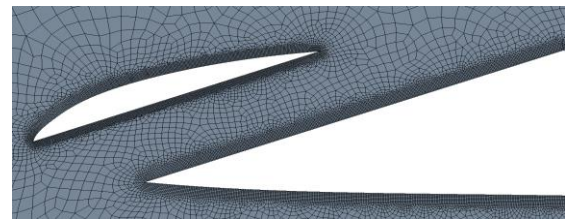
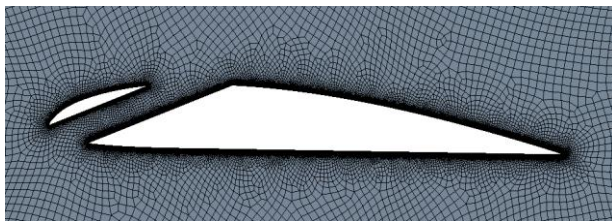


Figure 5. Slotted hydrofoil mesh detail.

Lift and drag coefficients are chosen as the parameters of interest for the mesh independence study. The mesh convergence is analysed based on the computations in the case of $\sigma = 0.7$ and $\alpha = 3^\circ$ on four sets of meshes with different resolution, as listed in Table 4. At $\sigma = 0.7$ (cloud cavitation regime), some specific features including vapor cloud shedding at the end of the cavity occurs. The wall distance of the first layer of grid nodes closest to the hydrofoil wall was set as 1×10^{-4} m for all the meshes.

A grid independence analysis has been done only for the non-slotted hydrofoil configuration for two main reasons: (i) For all configurations studied, the same domain size has been maintained; the modifications done only on hydrofoil surface (slot), and (ii) for the configuration with slot, a higher number of cells was used to mesh the slot walls and to assure that $y^+ \approx 1$, as can be seen in Figure 5.

Table 4. Mesh independence analysis.

Grid	Nodes	\bar{C}_L	Error (%)	\bar{C}_D	Error (%)
Coarse	27673	0.6246	-	0.0423	-
Medium	55561	0.5589	11.74	0.0370	14.31
Fine	233789	0.5401	3.50	0.0378	2.10
Very fine	307691	0.5353	0.89	0.0377	0.26

As can be seen, the time-averaged lift and drag coefficients have been used, since the cloud cavitation regime is not steady, and the time-average coefficients are more accurate and

representative. The absolute percentage change has been also calculated for the lift and drag coefficients. As can be observed from Table 4, the difference between the predicted lift and drag coefficients results decreases with increasing number of grid nodes. Table 4 shows that between the fine and very fine mesh the percentage change is negligible for both coefficients, however the number of elements is superior in the very fine mesh. Therefore, for the purpose of saving computational resources and time, the fine mesh was used for all subsequent calculations. As mentioned before, the fine mesh was also referenced as the base of the grid generation of the slotted hydrofoil.

4. Results and discussion

The time-averaged lift and drag coefficients of the Clark-Y hydrofoil for the range of cavitation numbers between 0.45 and 2.5 (from supercavitation, to cloud cavitation regime and non-cavitation) are illustrated in Figure 6. The time-averaged coefficients are calculated from the whole instantaneous results within one cavitation period, which makes the time-averaged values more accurate than instantaneous ones, since cavitation is not a steady phenomenon. To determine the shedding frequency of the cavitation phenomenon, we propose to apply a Fast Fourier Transform (FFT) to the lift coefficient. Figure 7 shows the L/D ratio for the same range of cavitation numbers.

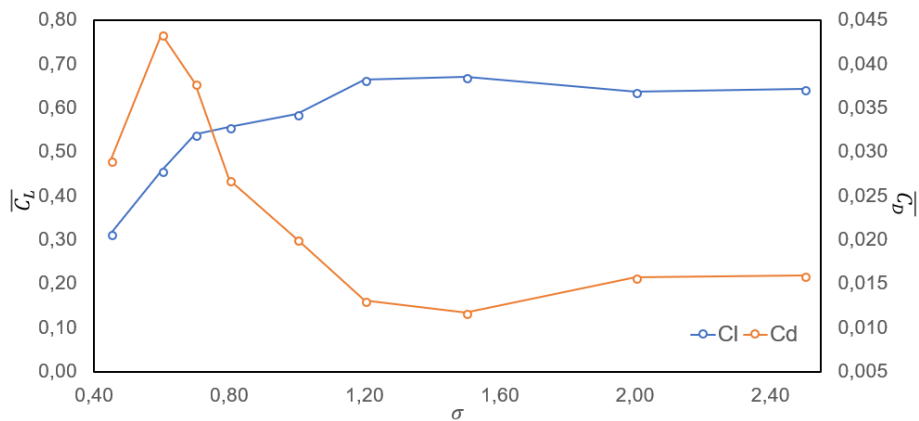


Figure 6. Time averaged lift and drag coefficients for different cavitation numbers.

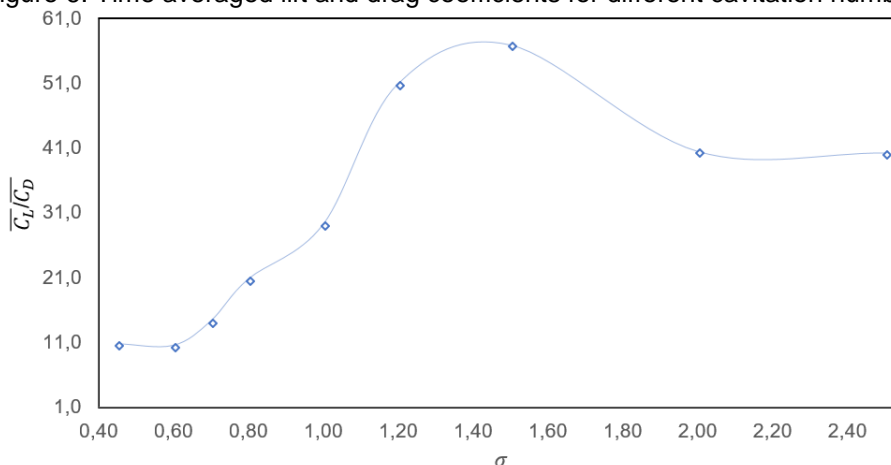


Figure 7. L/D ratio for different cavitation numbers.

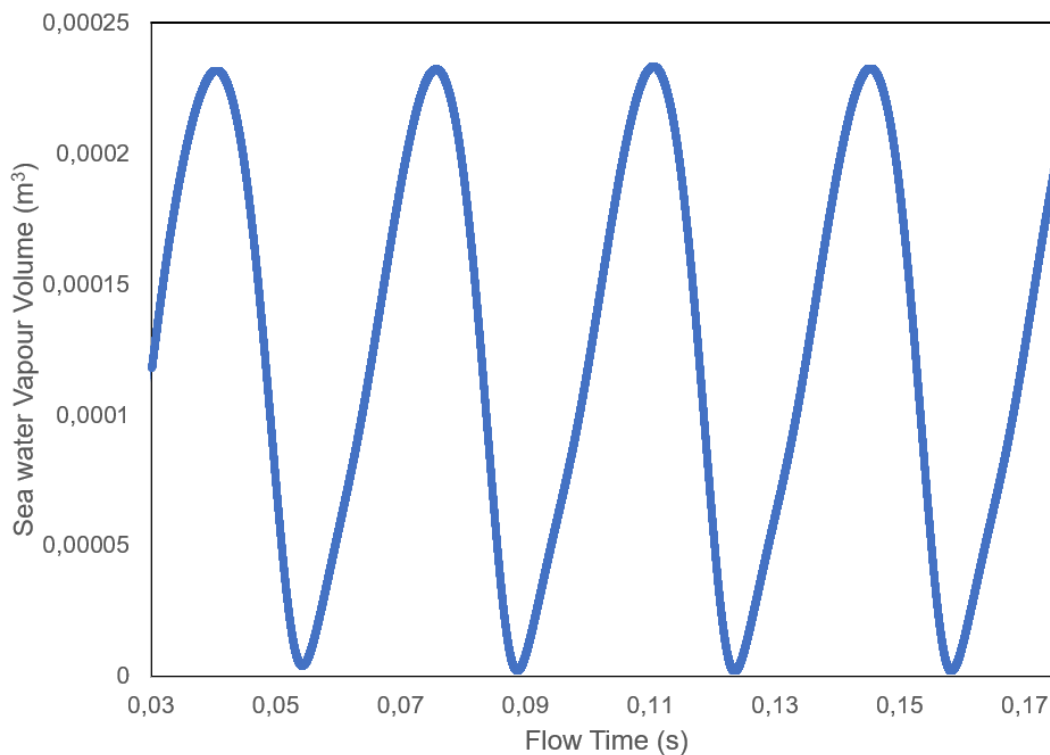
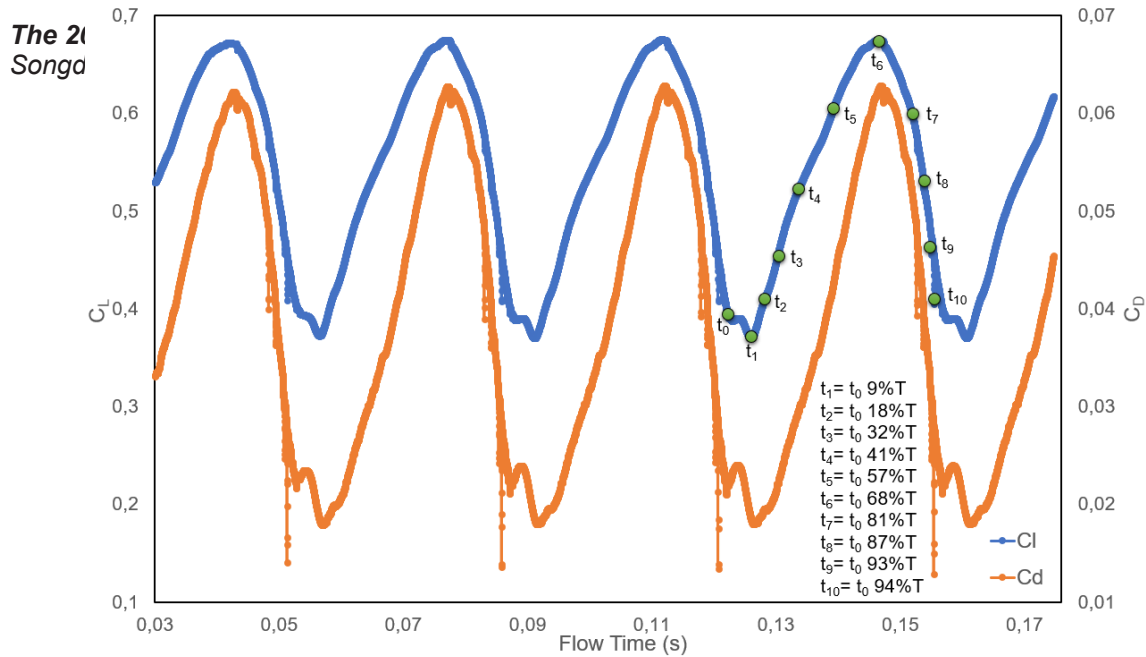
When the flow is non-cavitating (cavitation numbers larger than 1.9), both the lift and drag time-averaged coefficients remain practically unchanged as the cavitation number is varied, and thus the lift-over-drag ratio remains practically constant. In the cavitation inception stage (cavitation number 1.2-1.7) the net effect of cavitation on the lift and drag time-averaged coefficients is very small. As can be appreciated, there is a slight increase in the lift coefficient caused by the travelling bubbles in the inception cavitation stage. Further decreasing the cavitation number leads to the appearance of the sheet cavitation regime, which results in an increase of the drag coefficient and a decrease in the lift coefficient (which implies a high decrease in the L/D ratio, and thus a deterioration of the hydrodynamic performance). When the cavitation number drops below 0.9, the cloud cavitation regime appears. In this regime, the vortex shedding, and related flow unsteadiness strongly affects the flow structure around the hydrofoil, leading to the maximum of drag coefficient and minimum of lift, leading to a sharply deterioration of L/D. In the supercavitation regime (cavitation number less than 0.5) the lift coefficient continues to decrease however, the drag coefficients experiment a notably increase, and thus the L/D improve. However, in this study the supercavitation regime has not been considered for further analysis, since its applicability is out of the range of amphibious aircraft.

4.1 Time-dependent visualization of cloud cavity

As we are interested in the improvement of the cavitation performance of the hydrofoil, we will focus on cavitation number 0.7, as in these conditions the lift coefficient is minimum, and the drag coefficient is maximum, and thus the lift over drag ratio is negatively affected. Cloud cavitation is an undesirable phenomenon which significantly degrades the hydrodynamic performance and results in noise, erosion, and vibrations. A further analysis of this cavitation regime has been done. So, in this section details of the cloud cavitation regime over the Clark-Y hydrofoil are discussed.

Figure 8 illustrates the time evolution of the lift and drag coefficients. Both the lift and drag coefficients are seen to exhibit periodic behavior. Figure 9 shows the time evolution of the sea water vapor volume fraction. As can be observed, the volume variation is periodical and correlates with the lift and drag evolution. When the instantaneous values of the lift and drag coefficients are maximum, the vapor volume fraction also achieves the maximum volume.

To determine the major vortex-shedding frequency of the cavity phenomenon, a Fast Fourier Transform (FFT) can be applied to the time-history of the lift coefficient. In essence, the Fourier transform enables to take the time dependent data and resolve it into an equivalent summation of sine and cosine waves. The FFT has been applied using a prime-factor algorithm. Figure 10 shows the FFT analysis of for the C_L time-history. In Figure 10, the C_L FFT magnitude has been plotted in the ordinate axis. The magnitude (or amplitude) is the square root of the power spectral density (i.e. is the distribution of signal power in the frequency domain). From a deep analysis of Figure 10 it is possible to obtain the cavity shedding frequency, which is 28.635 Hz and a Strouhal number of $St = fc/V_\infty = 0.1694$ (where f is the shedding frequency and c denotes the hydrofoil chord). The cavity period is extracted from the shedding frequency as $T = 1/f = 0,034922$ s. From the cavity period it is possible to obtain the lift and drag time-averaged coefficients. To further evaluate the temporal evolution of the computational cavity structures and its consequences on the hydrodynamic performance, a study of the vapor volume fraction and pressure coefficient has been done (from t_0 to t_{10}) in one cavitation cycle. Sample points (from t_0 to t_4) has been expressed in percentage terms of the cavity period (as shown in Figure 8). Results are shown in Figure 11. Special attention will be paid to the correlation between the evolution of the vapor volume fraction and the pressure coefficient distribution along the hydrofoil surface.



Numerical results of the flow fields present strongly cyclic appearance. Figure 11 shows the filled contours of the vapor volume fraction, pressure coefficient and velocity magnitude at a series of moments (over one cavitation period). The study points have been expressed in terms of the cavitation shedding period (T) and have been illustrated in Figure 8. The cavitation is first triggered in the low-pressure region (hydrofoil upper surface), near the leading edge of the hydrofoil. The region covered by the cloud cavitation indicates that the local pressure is lower than the vapor pressure. As can be seen, the velocity magnitude contour shows that there is a low velocity region at the trailing edge of the hydrofoil. The region of low pressure continues its growth and makes the cavity growth downstream along the hydrofoil surface. In addition, the

pressure coefficient continues decreasing along the hydrofoil upper surface while the velocity magnitude increases, reducing the region of low velocity as the hydrofoil trailing edge.

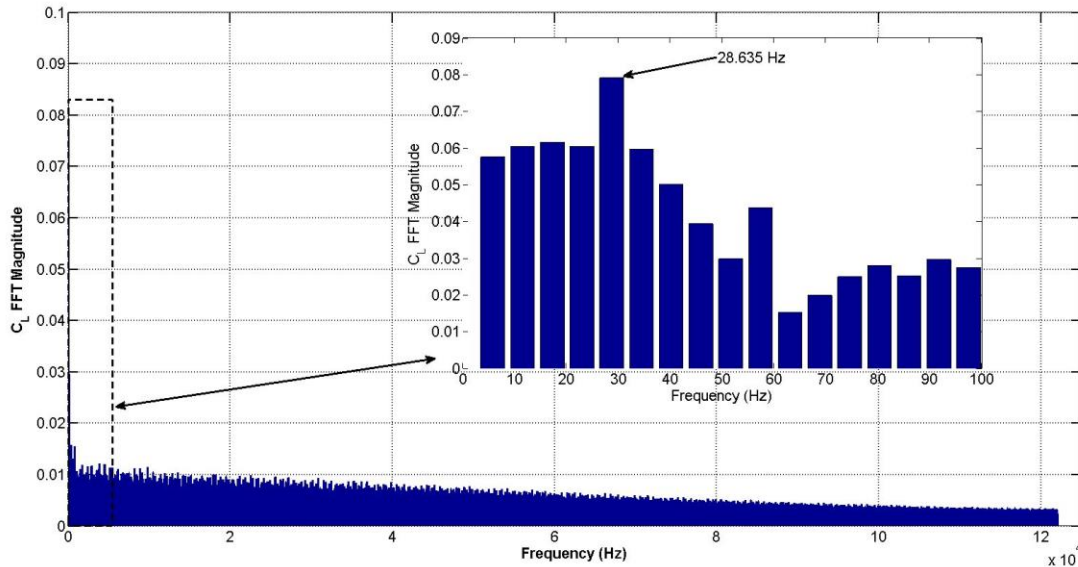
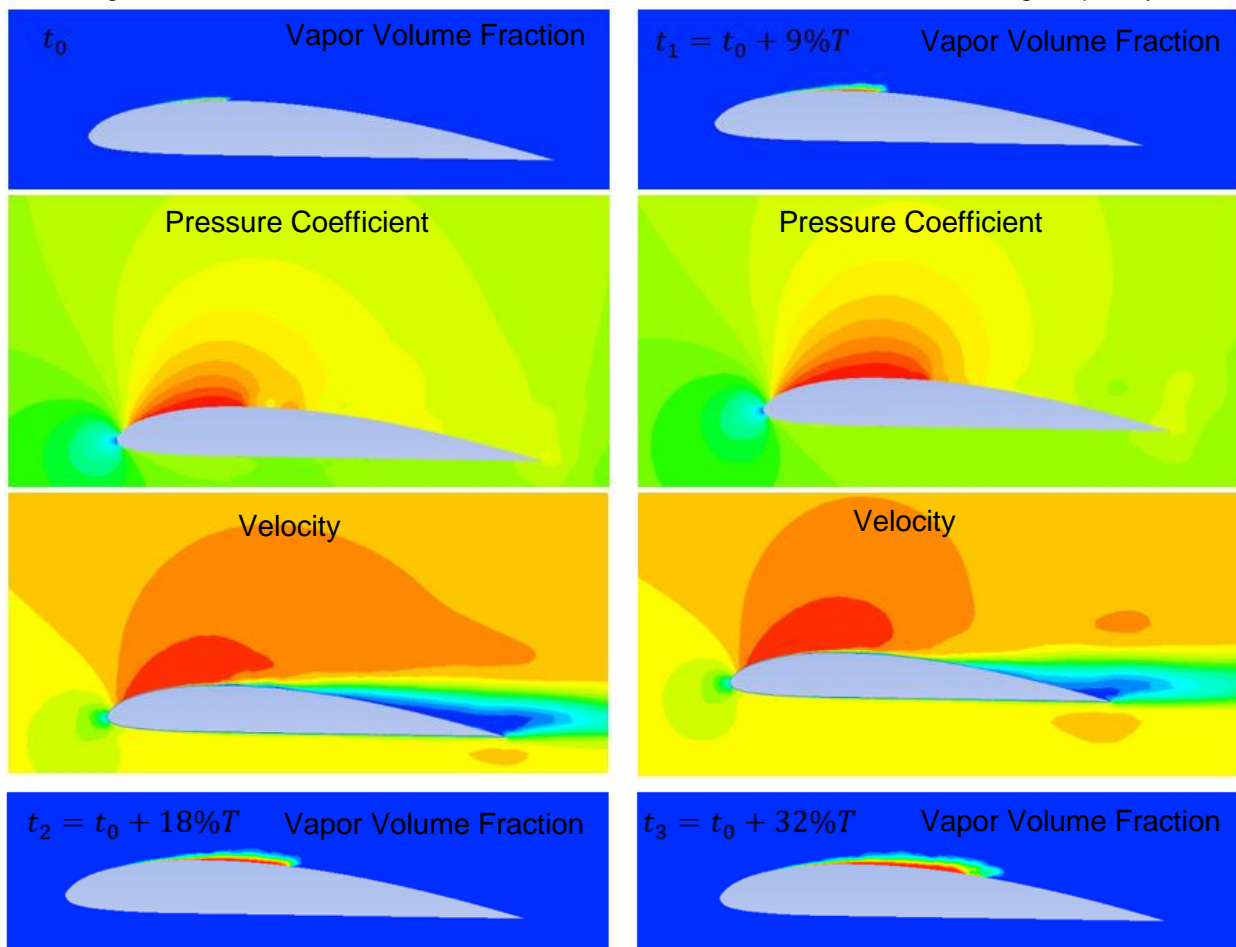
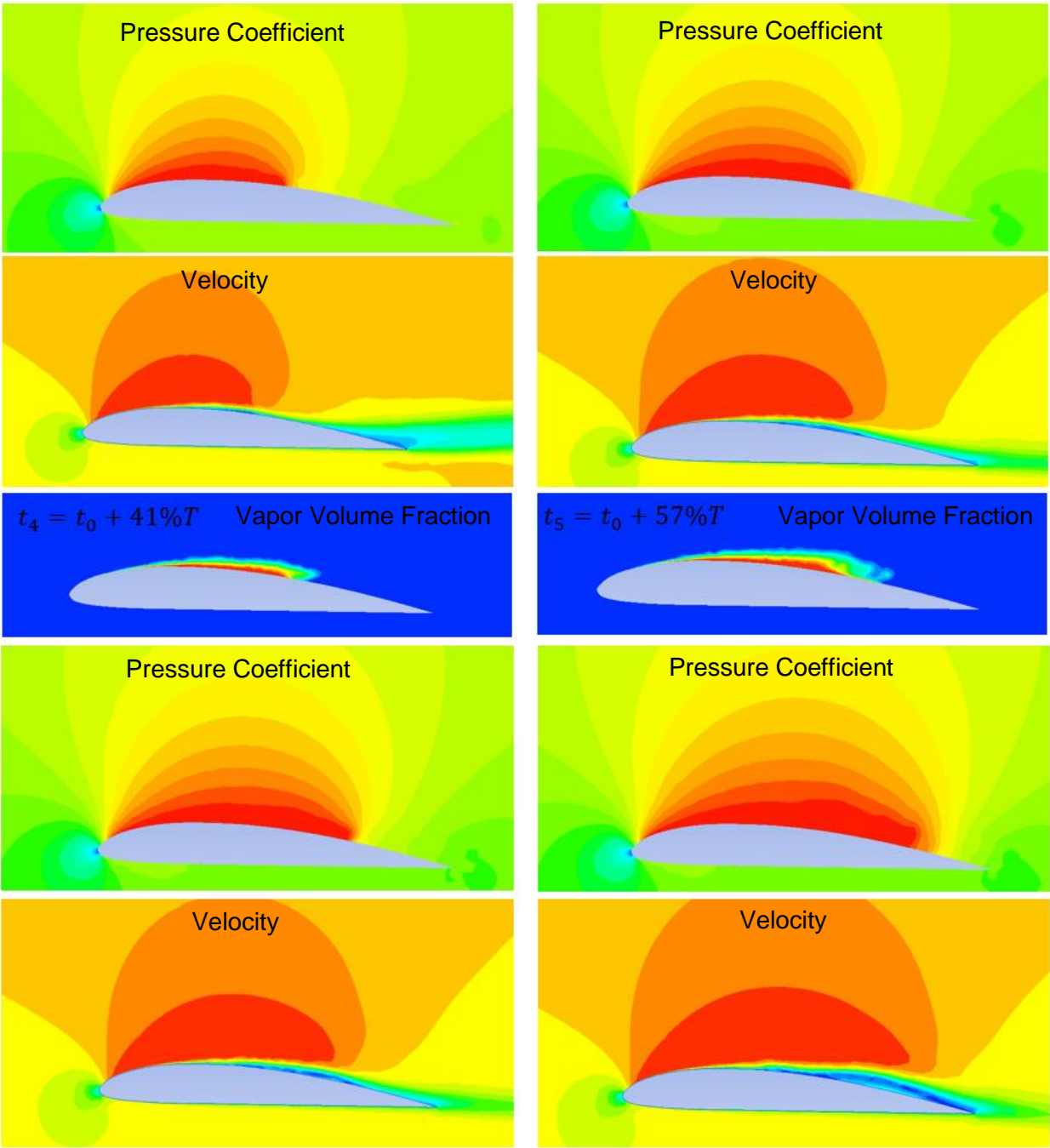
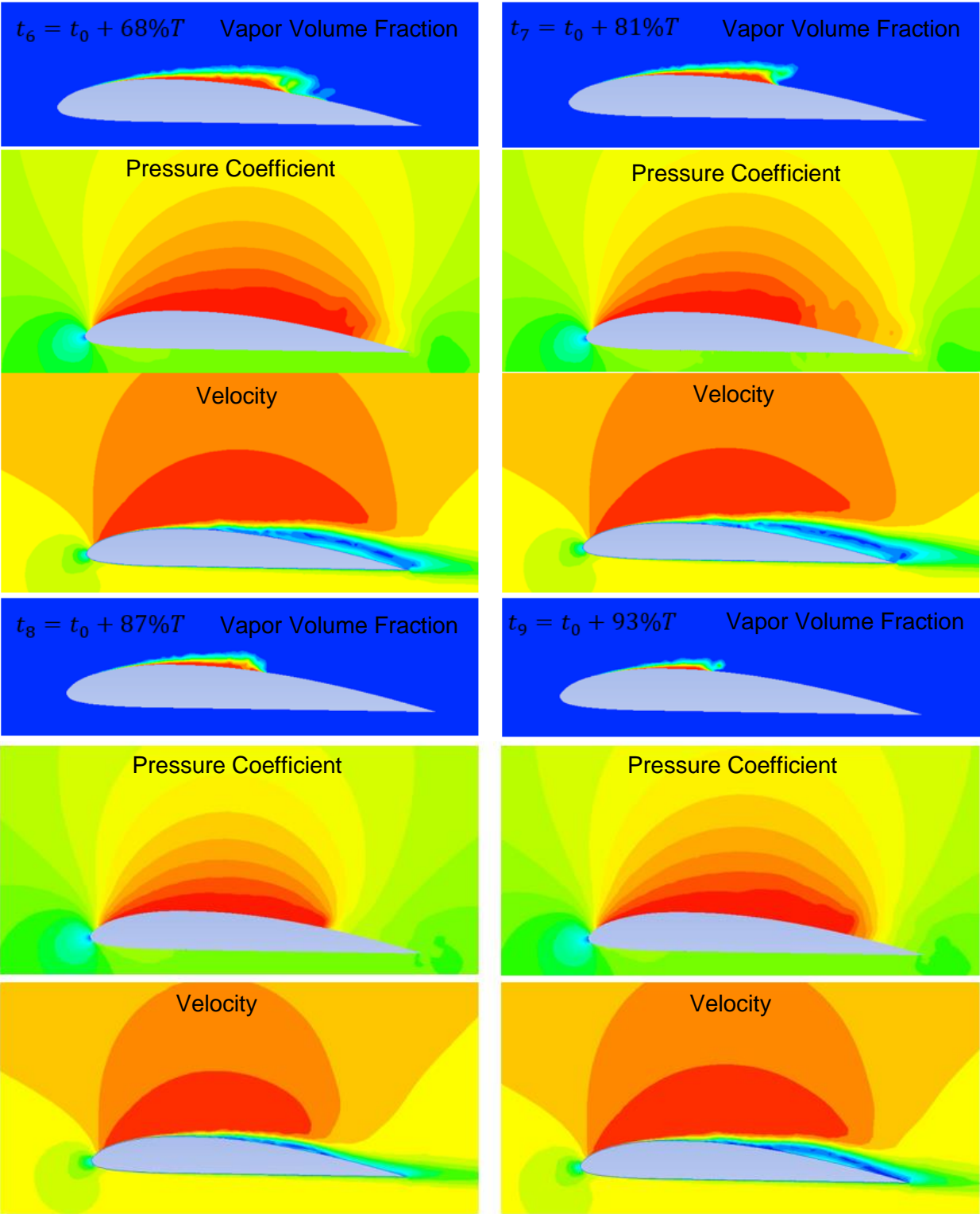


Figure 10. Fast Fourier Transform of the C_L coefficient and detail of the shedding frequency.







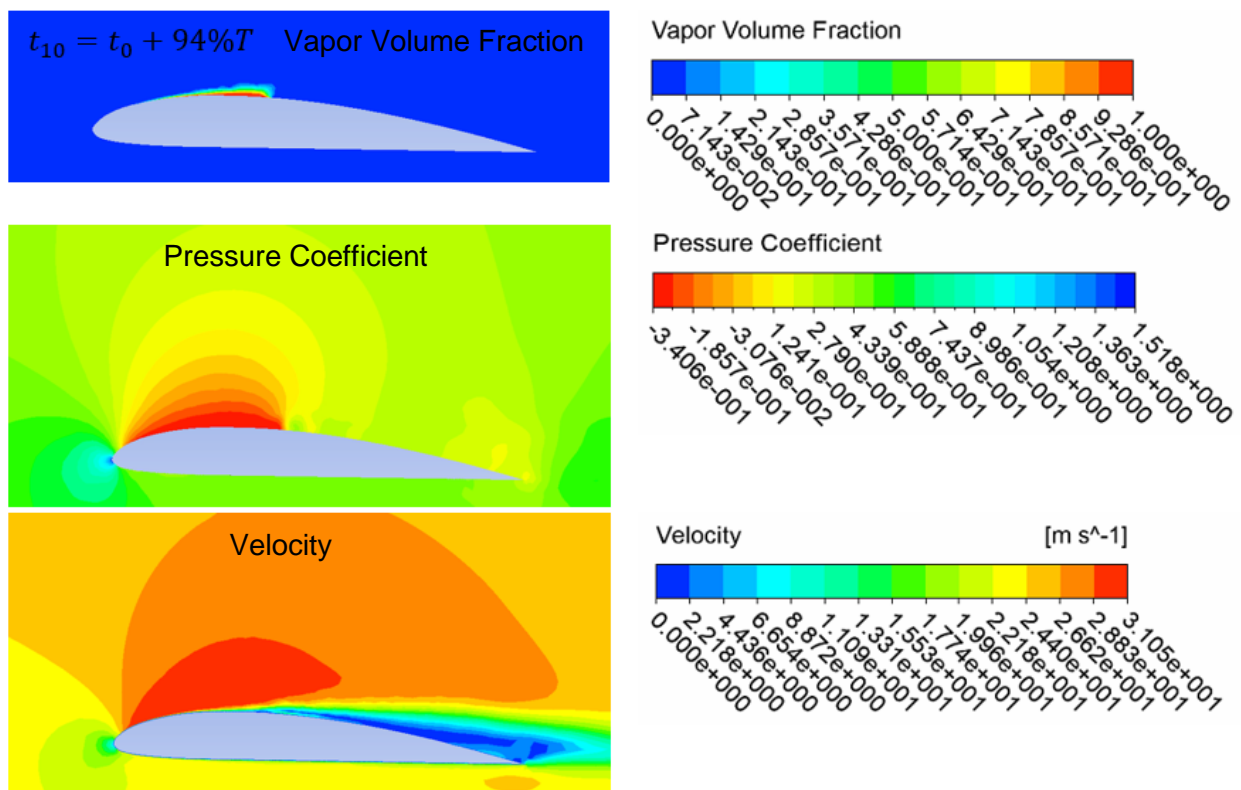


Figure 11. Vapor volume fraction, velocity, and pressure coefficients contours evolution over one cavitation cycle for cavitation number 0.7 (cloud cavitation regime).

When the cavity growth is more than half of the chord length (periods from t_5 to t_7) a re-entrant jet directed towards the hydrofoil leading edge appears (i.e. the pressure coefficient decreases along the rear part of the hydrofoil upper surface). The cavity structures are strongly affected by this re-entrant jet and it leads to the formation of a bubbly two phases mixture that breaks off from the rear part (in periods t_5 , t_6 and t_7 its possible to observe that there is a bubbly detachment). Although there is still cavity attached to the hydrofoil upper surface (close to the leading edge, in periods t_8 and t_9), it diminishes drastically due to the push effect caused by the relative high pressure downstream. In period t_{10} it is possible to observe that the cavity has reduced its presence to the half chord, the same behavior is observed in the pressure coefficient. After t_{10} , the almost vanished cavity regrows after the collapse, experimenting the same cyclic behavior.

5. Slotted hydrofoil numerical study

As has been described before the cloud cavitation regime affects the hydrodynamic performance and will lead to a poor take-off performance as well as undesired vibrations. In order to modify the flow structure which appears during cavitation phenomenon, control the bubble size and prevent erosion, a passive boundary layer control method has been proposed. Figure 11 describes the three design parameters of the slot. The angle θ allows to control the point where the flow coming through the slot arrives to the hydrofoil upper surface and thus modify the cavitation structures. In addition, parameters $L1$ and $L2$ allows to modify the width of the slot. Numerical simulations have been carried using the same setup described for the non-slotted configuration and the same domain dimensions and boundary conditions. As described in Section 3.3, the same mesh has been used, however a finer mesh has been used through

the slot wall to assure that $y^+ \approx 1$ and thus take full advantage of the of SST $k-\omega$ formulation. Moreover, the FFT has been applied to the C_L time-history in order to obtain the shedding frequency, and thus obtain the time-averaged lift and drag coefficients.

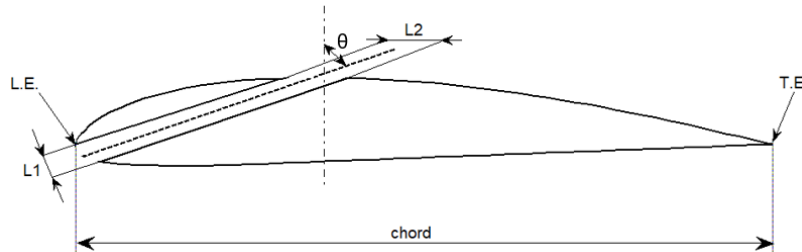


Figure 11. Slot geometric characteristics (L.E.: leading edge, T.E.: trailing edge, θ : slot angle).

Different slot locations, slot widths and angles have been numerically simulated to analyse the influence of this parameters on the cavitation performance. Table 5 summarizes the main cases configurations tested. As can be seen, the all the slotted configurations analysed improve the L/D ratio in comparison to the reference case (non-slotted hydrofoil) through the reduction of the vapor volume fraction and modification of the boundary layer. The use of lift and drag forces separately to determine the most suitable slot location is not appropriate as their variation may be in apposite directions with regards to objectives (increase lift and decrease drag). The variation of the lift-over-drag ratio with the slot design parameters is more meaningful for the study.

Table 5. Summary of the slotted/non-slotted numerical study.

Configuration	L1 (m)	L2 (m)	θ ($^\circ$)	L/D	Δ_v (%)
Base case	-	-	-	14.29	-
Parallel slot	0.0105	0.0105	79	19.91	-46
Convergent I	0.01	0.0055	75	20.27	-51
Convergent II	0.01	0.0055	82	21.38	-53
Divergent	0.007	0.017	80	15.74	-51

From Table 5 it is clear that the hydrodynamic and cavitating performance of the slotted hydrofoil is affected by the position of the slot. As shown in Table 5, the divergent configuration is the less suitable in terms of improving the hydrodynamic performance, this is due to the following reason: in a divergent duct (incompressible flow), the pressure increase but the velocity decreases, that is why this configuration still achieves a high reduction of the vapor volume fraction but has a poor L/D ratio, in other words, the fluid passing through the slot has not sufficient kinetic energy to re-energize the inner region of the boundary layer, where the main cavity structures appears. From Table 5, it can be inferred that the convergent slot configurations achieve a higher L/D ratio. Moreover, the effect of the slot in the vapor volume fraction reduction is affected by the inclination angle θ , due to the fact that the injection of fluid to re-energize the boundary layer is more effective near the point where the re-entrant jet appears, and thus where the bubbly two phases mixture break off. That is the reason why the convergent II configuration performs better than convergent I configuration (i.e. achieves a better hydrodynamic performance as well as a higher vapor volume fraction reduction).

6. Conclusions

We have discussed some of the design challenges of a hydrofoil from amphibious aircraft applications, focusing on the cavitation performance and its dire consequences during take-off performance. Numerical researches have been carried to simulate the cavitation performance of Clark-Y hydrofoil under a range of cavitation numbers. The Fast Fourier Transform (FFT) of the lift coefficient time-history has been used to obtain the cavity shedding frequency and to compute the lift and drag averaged coefficients over one period for different cavitation numbers. In addition, a further study of the cloud cavitation regime has been done, which shows that the evolution of the cavitation structures is correlated with the pressure distribution along the hydrofoil surface. In addition, the main mechanism of the cavity bubbles breakage is the re-entrant jet. So, modifications of the boundary layer could modify the cavity evolution. A passive boundary layer control method has been proposed. Three design parameters have been used to determine the influence of the slot location. Numerical results show that the slotted configuration not only could inhibit cavitation, it could also improve the hydrodynamic performance due to the boundary layer control. In order to revolutionize amphibious aircraft in general, more research efforts need to be invested to overcome the challenges, specially in water take-off performance. Through numerical simulation, it has been verified that the slot hydrofoil achieves a better hydrodynamic and cavitation performances at a fixed angle of attack. So, it has been proven that the slotted hydrofoil could be a potential method to improve take-off performance by reducing the dire effects of cavitation phenomenon.

7. Acknowledgments

The author gratefully acknowledges the support provided by Prof. Rhea P.Liem for all kind technical help and for all the time, valuable comments provided and fruitful discussions. The author would also like to thank Mr. Arjit Seth, a student at The Hong Kong University of Science and Technology, for the help and valuable comments provided during the numerical simulations.

Bibliography and References

- [1] Petrie, D. M., "Operational and Developmental Experience on the U.S. Navy Hydrofoil High Point" *Journal of Aircraft*, Vol. 3, No. 1, 1966, pp. 79-84.
- [2] John A. Mercier, "Tests of a Variable Sweep Hydrofoil with Cavitation and Ventilation" Davidson Laboratory, Letter Report 1332, January 1969.
- [3] Mikhail V. Timoshevskiy, Ivan I. Zapryagaev, Konstantin S. Pervunin, Dmitriy M., "Cavitating flow control through continuous tangential mass injection on a 2D hydrofoil at a small attack angle" *MATEC Web of Conferences* 84, 000 (2016).
- [4] M. Mortezaadeh, A. Katal, K. Javadi, "Cavitation Control on Hydrofoils" *Proceedings of the International Conference on Heat Transfer and Fluid Flow Prague, Czech Republic, August 11-12, 2014*.
- [5] Apparatus and Method for Reducing Hydrofoil Cavitation. (2005). US 2005/0076819 A1.
- [6] Dan M. Somers., "Design of a slotted, Natural-Laminar-Flow Airfoil for Business-Jet Applications". NASA/CR-2012-217559. Langley Research Center, July 2012.
- [7] R. Belamadi, A. Djemili, A. Ilinca, R. Mdouki, "Aerodynamic performance analysis of slotted airfoils for application to wind turbine blades" *Journal of Wind Engineering and Industrial Aerodynamics*, 151 (2016) pp. 79-99.

- [8] W. Qun, C. Hong-xun, Z. Rui, "Numerical Research on the Performances of Slot Hydrofoil" *Journal of Hydrodynamics*, 27, 2015, pp. 105-111.
- [9] L. Qiu, W. Song, "Efficient Decoupled Hydrodynamic and Aerodynamic Analysis of Amphibious Aircraft Water Takeoff Process" *Journal of Aircraft*, Vol. 50, No. 5, September–October 2013.
- [10] Eppler, Richard, and Young T. Shen. "Wing Sections for Hydrofoils, Part 2: Nonsymmetrical Profiles" *Journal of ship research* 25.3 (1981).
- [11] S.A. Oller, L. G. Nallim., "Usability of the Selig S1223 Profile Airfoil as a High Lift Hydrofoil for Hydrokinetic Application". *Journal of Applied Fluid Mechanics*, Vol. 9, No. 2, pp. 537-542, 2016.
- [12] N. arg, Gaetan K.W. Kenway., "High-fidelity multipoint hydrostructural optimization of a 3-D hydrofoil". *Journal of Fluids and Structures* 71 (2017), pp. 15–39.
- [13] Kirill V. Rozhdestvensky., "Wing-in-ground effect Vehicles". *Progress in Aerospace Sciences* 42 (2006), pp. 211–283.
- [14] S. P. Iliev, "Aerofoil Analysis using XFOIL", Imperial College London, Department of Aeronautics, 2016.
- [15] S. Phoemsapthaweea, J.B. Leroux, S. Kerampranb, J.M. Laurens, "Implementation of a transpiration velocity-based cavitation model within a RANSE solver", *European Journal of Mechanics B/Fluids* 32 (2012) pp. 45–51.
- [16] A. Šarc, T. Stepišnik-Perdih., "The issue of cavitation number value in studies of water treatment by hydrodynamic cavitation". *Ultrasonics Sonochemistry* 34 (2017), pp. 51–59.
- [17] E. Roohi, A.Pouyan Zahiri., "Numerical simulation of cavitation around a two-dimensional hydrofoil using VOF method and LES turbulence model". *Applied Mathematical Modelling* 37 (2013), pp. 6469–6488.
- [18] N. Garg, Gaetan K.W. Kenway., "High-fidelity multipoint hydrostructural optimization of a 3-D hydrofoil". *Journal of Fluids and Structures* 71 (2017), pp. 15–39.